

Retrieval of upper stratospheric and mesospheric temperature profiles from Millimeter–Wave Atmospheric Sounder data

A. von Engeln,¹ J. Langen, T. Wehr

Earth Sciences Division, European Space Research and Technology Center, Noordwijk, Netherlands.

S. Bühler, K. Künzi

Institute of Remote Sensing, University of Bremen, Bremen, Germany.

Abstract. The Millimeter–Wave Atmospheric Sounder (MAS) is a shuttle–based instrument, observing the atmosphere in limb sounding geometry. Temperature information is derived from three oxygen lines near 60 GHz. Temperature profiles in the altitude range from 30 to 90 km can be measured. The data evaluation is done with the aid of an atmospheric radiative transfer model. Usually, the radiation is assumed to be unpolarized, so that spectral power is a scalar quantity. This assumption is not valid for oxygen lines that show Zeeman splitting in the Earth’s magnetic field. A more general form of the radiative transfer in which spectral power is represented by a vector has to be used in this case. The obtained information depends on the magnetic field. Using the MAS instrument characteristics, we investigate the possible temperature information that can be obtained from observation of polarized O₂ emission lines with a spaceborne instrument. Synthetic retrievals show that the obtained accuracy of the retrieved temperature profile is below 3 K from 30 to 55 km and below 6 K for altitudes up to 90 km. The resolution is 4 km for altitudes of 30 to 50 km and 10 km above. The magnetic parameters influence the accuracy of the obtained profile by as much as 2 K. The obtained MAS temperature profiles were validated by a comparison to data from the Upper Atmosphere Research Satellite (UARS). Three UARS instruments were chosen: Microwave Limb Sounder, Improved Stratospheric and Mesospheric Sounder, and the Cryogenic Limb Array Etalon Spectrometer. All comparisons show similar features for the stratospheric and mesospheric temperatures.

1. Introduction

Atmospheric temperature is the single most important parameter when dealing with the atmosphere in areas such as meteorology, photochemistry, or climatology. The most accurate way to determine atmospheric temperature remotely is by measuring the thermal emission at an appropriate wavelength. However, one has to be careful to ensure that

local thermodynamic equilibrium (LTE) is fulfilled in the atmospheric layers from which the radiation originates. Since the existence of LTE depends heavily on pressure and wavelength, it is important to select the observing wavelength accordingly. For observations in the thermal infrared range (near 10 μ m wavelength), LTE generally holds to \approx 50 km altitude. For the microwave range, for example, near 5 mm wavelength, the LTE is valid up to 100 km. The Millimeter–Wave Atmospheric Sounder (MAS) is the first and so far only instrument offering the capability to obtain direct temperature measurements all the way up into the upper meso-

¹now at Institute of Remote Sensing, University of Bremen, Bremen, Germany.

sphere.

MAS measures thermal emissions from oxygen resonance lines near 60 GHz since O_2 has a known volume mixing ratio over the considered altitude range (usually 0–100 km) and a strong line spectrum. Because of its magnetic dipole moment, O_2 interacts with the Earth's magnetic field. This leads to Zeeman splitting of the oxygen lines. The modeling of this effect requires a polarized radiative transfer calculation through the atmosphere. Both the position of the sensor and the tangent point have to be taken into account with respect to the strength and direction of the magnetic field.

Below 50 km an unpolarized approximation for the radiative transfer is valid if information from the line center (± 10 MHz) is omitted. This is possible since most of the information can be acquired from the line shape, which at these altitudes is dominated by pressure broadening. MAS temperature inversions where this approximation was applied can be found in the work of *Wehr et al.* [1998]. The influence of the Zeeman splitting above 50 km cannot be neglected.

The MAS observes the limb at right angle to the flight direction of the shuttle. The latitudinal coverage is either 70° N to 40° S or 70° S to 40° N, depending on the shuttle orientation. The duration of one scan cycle corresponds to a ground distance of ≈ 100 km. An instrument description can be found in the work of *Croskey et al.* [1992].

The instrument was operated during the Atmospheric Laboratory for Applications and Science (ATLAS) missions 1 (March 24 to April 2, 1992), 2 (April 8 – 17, 1993), and 3 (November 3 – 14, 1994). The main aims of the ATLAS missions were atmospheric science, solar science, space plasma physics, and ultraviolet astronomy. The MAS instrument was part of the atmospheric science payload, studying the chemistry and physics of the upper atmosphere.

The MAS is a passive microwave instrument, using heterodyne technique to measure the atmospheric radiances at certain frequencies. Temperature, ClO, O_3 , and H_2O profiles can be obtained. It observes the 61.151 GHz oxygen line with high resolution for the temperature measurement and the oxygen lines located at 62.998 and 63.569 GHz with lower resolution. The frequency resolution of the MAS oxygen filters is given in Table 1; the coverage of the filters is symmetric around the line center.

The two lines with lower resolution are mainly needed for a correction to the tangent altitude information coming from the shuttle navigation system. This correction is performed with information extracted from the shape of these lines at tangent altitudes ranging from 30 to 50 km [*Berg, 1995*]. The shape of these lines in this altitude region is

dominated by pressure broadening, and the high-resolution filters of the temperature line are not necessary. These lines can also be used for temperature measurements; however, the 61.151 GHz line has better coverage in the mesosphere, mainly owing to the high-resolution filters and the higher intensity of this line.

The O_3 profiles are obtained from the 184.377 GHz line, H_2O profiles are obtained from 183.310 GHz, and ClO profiles are obtained by using the 204.352 GHz line. Retrievals of these profiles were already performed by *Hartmann et al.* [1996], where a combination of model and meteorological data was used for the temperature profile.

2. The Forward Model

The radiative transfer or so-called Forward model F calculates the spectral power observed by the instrument for a given state of the atmosphere. It includes the instrument characteristics like antenna pattern, filter response curves, and receiver sideband efficiency. The output of F is used by the inverse model to find the best approximation to the atmospheric temperature profile in an iterative process.

The line spectrum of O_2 around 60 GHz is the result of spin flip transitions at different rotational levels. The spin S results from two unpaired electrons leading to $S = 1$ for the O_2 molecule. The orbital angular momentum is zero, and the spin angular momentum is coupled to the rotational angular momentum through a weak magnetic field arising from the molecular rotation. This coupling can be approximated by a Hund's case b [*Gordy and Cook, 1970*]. The vector addition of S and the rotational quantum number N leads to a total of three levels of the total angular momentum J per rotational level. Two different transitions are of importance for the considered frequency range: from the $J = N$ to the $J = N + 1$ level (designated as $N+$ lines) and between the $J = N$ and the $J = N - 1$ level (designated as $N-$ lines). Only odd N values are allowed because of the symmetry requirements. Each J level will split up into $(2J + 1)$ sublevels when applying a magnetic field.

The sublevels are classified according to their magnetic quantum number M_J . Only transitions which follow the selection rules $\Delta M_J = 0, \pm 1$ are allowed. The line name convention is as follows: $\Delta M_J = +1 \equiv \sigma^+$ lines, $\Delta M_J = -1 \equiv \sigma^-$ lines, $\Delta M_J = 0 \equiv \pi$ lines. The polarization and intensity of the Zeeman split lines change with the direction of the magnetic field. In total, there are $3(2N + 1)$ transitions for the $N+$ lines and $3(2N - 1)$ transitions for the $N-$ lines. This leads to a total number of 57 Zeeman lines when considering the $9+$ line at 61.151 GHz.

At microwave frequencies it is customary to express the emitted intensity in equivalent brightness temperatures (BT)

Table 1. MAS Oxygen Filter Channels

O ₂ Line	Bandwidth	Number of Filter Channels		
		40 MHz	2 MHz	0.2 MHz
61.151 GHz	400 MHz	10	20	20
62.998 GHz	400 MHz	10	20	—
63.569 GHz	400 MHz	10	20	—

by dividing the intensity with Boltzmann's constant. The BT is usually described as a scalar in the radiation transfer equation, but this simplification does not hold for oxygen lines in the presence of a magnetic field [Lenoir, 1967]. Lenoir [1967] discussed the influence of the magnetic field on the BT of microwave O₂ lines at a given frequency ν and showed that the radiative transfer through a homogenous layer in the Rayleigh–Jeans approximation can be written as

$$\mathbf{T}_{\mathbf{B}}(z, \nu) = e^{-\mathbf{G}z} \mathbf{T}_{\mathbf{B}}(0, \nu) e^{-\mathbf{G}^\dagger z} + T(\mathbf{I} - e^{-\mathbf{G}z} e^{-\mathbf{G}^\dagger z}) \quad (1)$$

where $\mathbf{T}_{\mathbf{B}}$ is a 2×2 matrix describing the BT in the polarized case. The path length is given by z , \mathbf{I} is the identity matrix, \mathbf{G} stands for the complex propagation tensor (dimension 2×2), $\mathbf{T}_{\mathbf{B}}(0, \nu)$ is the incident BT, T is the physical temperature of the atmosphere, and the dagger symbol denotes the conjugate transpose. The diagonal elements of $\mathbf{T}_{\mathbf{B}}$ give the BT in the corresponding polarization basis; the off-diagonal elements give the coherency.

The received radiation is generally elliptically polarized, where the polarization and the intensity of the Zeeman lines depend on the angle between the direction of the magnetic field and the propagation direction Φ . An angle of $\Phi = 0^\circ$ (observing parallel to the field) will reveal the σ^+ and σ^- lines, both circular polarized. Perpendicular observation ($\Phi = 90^\circ$) will reveal all three lines linear polarized; the emitted linear component of the electric field of the σ lines is oriented along the magnetic field, and the one of the π lines is perpendicular to it. All other angles lead to a superposition of the σ and π lines resulting in elliptical polarization.

The complex propagation tensor \mathbf{G} can be calculated according to

$$\mathbf{G}(\nu) = a \left[\mathbf{I} + \sum_{\Delta M=-1}^1 \mathbf{P}_{\Delta M}(\Phi) \sum_{M_J} A_{M_J, \Delta M}(\nu) \right] \quad (2)$$

where $a = i2\pi\nu/c$, c is the speed of light, and \mathbf{P} describes the polarization as a function of ΔM and Φ . The magnetic quan-

tum number of the upper energy level is given by M_J , which is the $J = N$ level for both the N^+ and the N^- transition [Rosenkranz, 1993], and A denotes the complex refractivity of a certain Zeeman transition.

The matrix \mathbf{P} in a linear polarization basis has been formulated by Lenoir [1968]. A linear polarization basis proves to be convenient for the MAS since the MAS observes a linear component of the emitted radiation.

The complex index of refraction A is given by

$$A_{M_J, \Delta M}(\nu) = S \xi_{M_J, \Delta M} F_{M_J, \Delta M}(\nu, \nu_{fi}) \quad (3)$$

in which S stands for the line strength of the unsplit line and $\xi_{M_J, \Delta M}$ stands for the relative intensity of the considered Zeeman line, depending on M_J and ΔM . $F_{M_J, \Delta M}$ is the line shape factor, ν and ν_{fi} are the frequencies where the calculation is performed and the center frequency of the Zeeman component, respectively. The frequency ν_{fi} depends on the strength of the magnetic field. Formulas that calculate ν_{fi} and ξ can be found in the work of Rosenkranz [1993], expressions calculating S are available in the work of Liebe and Hufford [1989], and a suitable approximation to F is published in the work of Hui *et al.* [1978].

The frequency shift $\Delta\nu$ in Megahertz of the N^+ lines for the σ^\pm transitions can be calculated according to Rosenkranz [1993]:

$$\Delta\nu = 0.028026 B \frac{M(N-1) \pm N}{N(N+1)} \quad (4)$$

where B is the magnetic strength in microtesla. Applying equation (4) to the 9+ line and a maximum expected magnetic field strength of $66 \mu\text{T}$ yields a maximum frequency shift of ± 1.66 MHz from the unsplit line center. The frequency shift for the π lines is lower. Thus the high-resolution filters of the MAS cover the magnetically split line.

The frequency difference $\Delta\nu_{\text{diff}}$ in Megahertz between

two Zeeman lines of the same ΔM_J is for the $N+$ lines,

$$\Delta\nu_{\text{diff}} = 0.028026 B \frac{N-1}{N(N+1)} \quad (5)$$

Applying this to the $9+$ line with a typical magnetic field strength of $50 \mu\text{T}$ yields a spacing of 0.125 MHz for the Zeeman lines. The width of the narrow MAS filters is 200 kHz ; hence it is not possible to resolve single lines.

The atmosphere is divided into homogeneous layers of 1 km thickness for the calculation of the emerging brightness temperature at the top of the atmosphere. The received signal is a sum of emissions from each layer, partially absorbed by subsequent layers.

Since the observed signal depends on the magnetic field, it is necessary to take the variation of the magnetic field along the observation path into account. The calculation of the \mathbf{G} matrix is done in vertical steps of 1 km along the integration path. Calculating the magnetic field for each of these integration points would slow down the program considerably. It is justified to use a linear interpolation scheme since the magnetic field strength and angle variations with the geographic positions are generally slow (as can be seen in Figures 1–13 by Barraclough [1986]), except when close to the magnetic poles.

The magnetic parameters are obtained from the International Geomagnetic Reference Field (IGRF) model [Barraclough, 1986]. They are calculated at the tangent point location and, in addition, at the geographic locations where the integration path reaches an altitude of 120 km . The atmospheric signal from altitudes above 120 km is negligible. In total, the field is calculated at three different locations along one integration path. One MAS scan through the atmosphere is simulated by the calculation of the magnetic field at tangent altitudes from 0 to 120 km in vertical steps of 1 km , so that there are in total 361 magnetic field parameters calculated for one scan. Linear interpolation is used for all points lying in between; the maximum angle between these reference points occurs at a tangent altitude of 0 km and is 11° great circle distance.

The calculation of the absorption coefficients in the scalar radiation transfer equation is done only once since they do not depend on the geographic location. Approximating the magnetic field with the values at the tangent point and calculating the polarized absorption coefficients only once is not possible because the magnetic field can vary by more than 10% within the integration path. Therefore the polarized absorption coefficients for the oxygen line of interest are calculated during the integration along the path. All other lines, including other oxygen lines, can be calculated unpolarized and will add equal quantities to the diagonal elements of the \mathbf{G} matrix. In order to optimize the program, only BT for fre-

quencies $\pm 27 \text{ MHz}$ around the oxygen line center are calculated polarized since the polarization decreases with the distance from the line center. All other frequencies are calculated unpolarized. This approximation leads to errors $< 1\%$ in the calculated BT.

The effect of the instrumental resolution is visualized in Figure 1. The influence of the instrument characteristics leads to higher observed BT in the wings of the line owing to the finite width of the antenna pattern, a factor of ≈ 0.5 in the total BT due to sideband convolution, and a poorer frequency resolution due to the filter integration.

The dip in the center of the line at a tangent altitude of 70 km results from the signal at altitudes of $\approx 80 \text{ km}$, where the line saturates. The measured BT is, in this case, equal to the physical temperature of the atmosphere, when no instrument characteristics were applied. The BT is lower because of the lower temperature at 80 km . The dip disappears at an altitude of 80 km , and the influence of the magnetic field dominates the line shape. The fine structure within $\pm 2 \text{ MHz}$ around line center results from the individual σ and π lines (Figure 1, top) and cannot be resolved by the MAS (Figure 1, middle). The overall shape (interval $\pm 2 \text{ MHz}$ around line center) will be concave (σ lines are more pronounced), convex (π lines are more pronounced), or flat (either superposition of π and σ lines or radiation is unpolarized and emerging from one altitude level). The unpolarized BT in Figure 1 (bottom) reveal a much smaller dip in the center and show a smaller half width at half maximum. The signal is stronger than that in the polarized case for altitudes where the line is not saturated ($\geq 90 \text{ km}$) because all oxygen molecules radiate at the center frequency.

The broadening of the line due to the magnetic fields is negligible below 50 km , and it is possible to treat the emission unpolarized by excluding the center filters. This exclusion could be avoided by the introduction of a new line shape. This shape will include, beside the pressure and Doppler broadening, an additional broadening parameter owing to the magnetic field. Thus unpolarized retrievals can be performed. The upper altitude limit for this new line shape varies with the magnetic strength because the approximation does not work if the signal is dominated by polarized emissions. The limits for magnetic strengths of 30 and $50 \mu\text{T}$ are 85 and 80 km , respectively.

Although the MAS observes only a linear component of the emitted radiation, the influence of polarization cannot be neglected. The degree of polarization P can be calculated as

$$P = \sqrt{1 - \frac{4|\mathbf{T}_B|}{(\text{Tr}(\mathbf{T}_B))^2}} \quad (6)$$

where $|\mathbf{T}_B|$ denotes the determinant of \mathbf{T}_B and Tr stands for

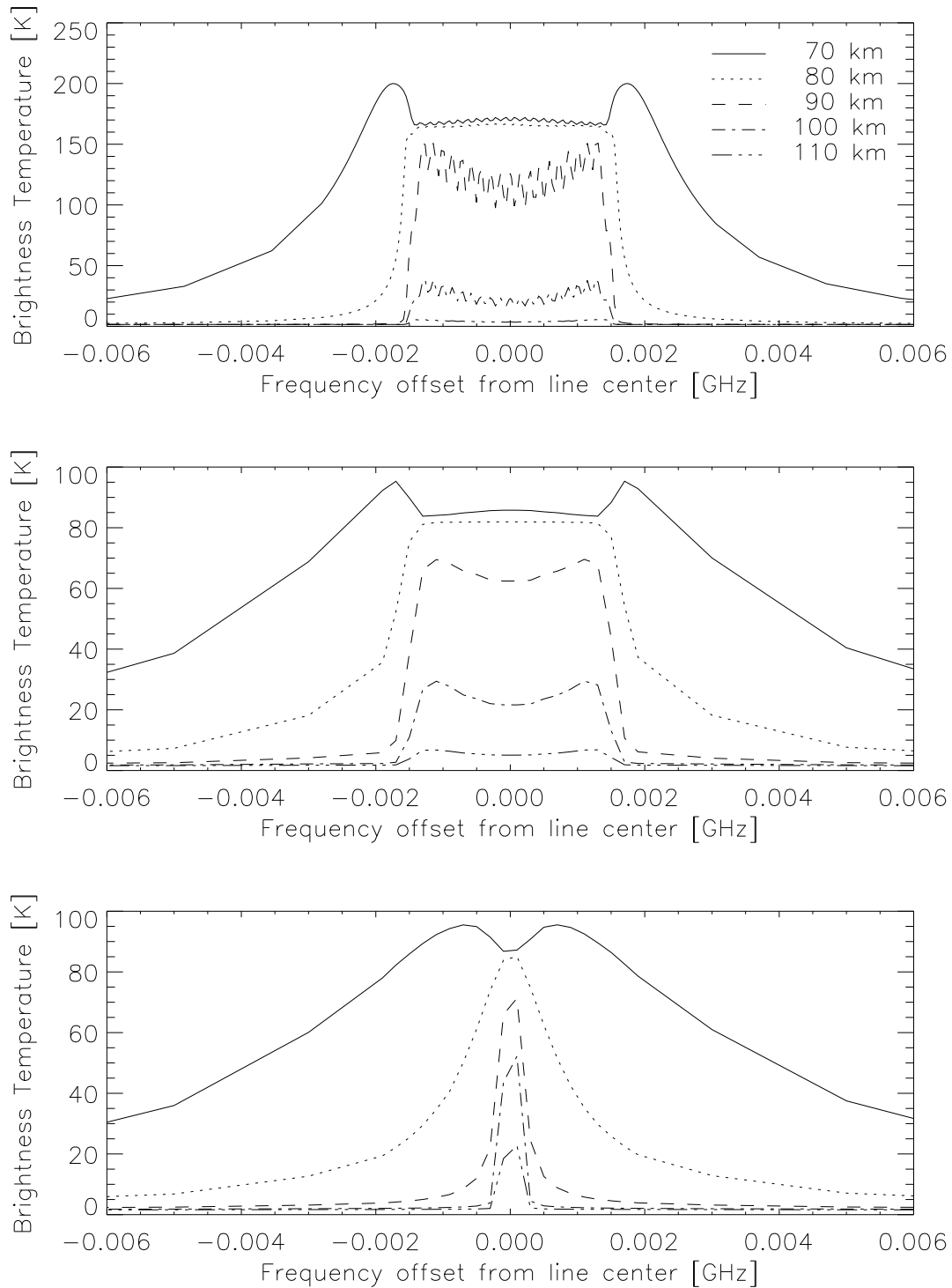


Figure 1. Simulated brightness temperatures for tangent altitudes 70–110 km, including (top): the linear component of the spectrum which is observed by the Millimeter–Wave Atmospheric Sounder (MAS), where no instrument characteristics have been applied, (middle): the BT of the top simulation with instrument characteristics applied, and (bottom): the hypothetical unpolarized case with instrument characteristics applied. The mean location of the tangent point is as follows: 133°E, 65°N; $B = 58 \mu\text{T}$, and $\Phi = 98^\circ$. The legend in Figure 1 (top) indicates the altitude levels.

the trace. The degree of polarization changes with frequency and altitude; the higher the tangent point, the higher the degree of polarization.

The influence of the magnetic field on the polarization P is shown in Figure 2. Figure 2 (top) shows the dependence of P on the magnetic field strength B . The polarization in the case of $B = 0 \mu\text{T}$ is zero, and the emitted radiation is unpolarized. The σ lines move farther away from line center with increasing B , and the π lines in the center become visible. The overlapping of σ and π lines at line center leads to low polarization. The σ lines possess higher polarization because the influence of the π lines decreases with distance from line center, while the σ line intensities increase. The situation for different angles Φ is presented in Figure 2 (bottom); the magnetic field is calculated according to the model and is $\approx 58 \mu\text{T}$. At an angle of 0° only the σ lines are visible; increasing the angle allows the observation of the π lines around line center and a decrease of the σ line polarization due to superposition of the π and σ lines.

The MAS observes a linear component of the emitted electric field, where the orientation is along the scan direction. Therefore the received spectrum does not only depend on the magnetic field parameters but also on the angle Θ between the projected magnetic field in the plane perpendicular to the integration path and the scan direction in this plane since the coordinate system for the emitted ellipse is established by this projection. The angle Θ is calculated from the magnetic field parameters at 120 km, where the atmospheric signal emerges because the linear polarization basis follows the magnetic field along the integration path.

The dependence of the received BT on the magnetic field strength is shown in Figure 3 (top). An increasing magnetic field leads to a broadening of the observed line. The $0 \mu\text{T}$ calculation has the highest BT in the center because all O_2 molecules are emitting and absorbing at the center frequency, and the line saturates at altitudes with higher temperatures above the mesopause. (The mesopause for this model atmosphere is at ≈ 90 km.) The calculations with a magnetic field strength $> 0 \mu\text{T}$ show similar BT around the center of the line because the line saturates at similar altitudes below the mesopause. Moving the tangent point farther down will reverse the picture because the integration path through the atmosphere changes. This will lead to a lower saturation point. Hence the $0 \mu\text{T}$ calculation will have lower BT while the other calculations will have higher ones, as a result of the different signs of the temperature gradients above and below the mesopause.

The influence of the angles Φ and Θ on the received BT can be seen in Figure 3 (middle and bottom). Both cases are identical for the 0° calculation, where the σ lines are circular polarized, and the measured intensity in any linear polariza-

tion basis is identical. With an increasing angle the σ lines are elliptically polarized, and at an angle of 90° linear, they are oriented along the magnetic field lines. The high polarization of the σ lines and the alignment of these lines along the magnetic field lead to an increase of the observed BT and to a doubling of the measured BT at ± 1.5 MHz from line center in the $\Theta = 0^\circ$ case. The polarization of the signal in the center is low since the contribution to the polarization at the line center comes mainly from the π lines (see Figure 2). The signal in the center is not saturated, and the increase of Φ leads to a higher intensity. A lower tangent point would lead to identical BT at line center for all angles because the line saturates just below 80 km.

The line width in the $\Theta = 90^\circ$ case for $\Phi > 0^\circ$ is smaller than that in the $\Theta = 0^\circ$ case because the influence of the σ lines is weaker. The plateau in the center widens with angle owing to the increasing influence of the π lines. The observed BT in the center is decreasing with angle since the influence of the π lines leads to higher absorption, and thus the line saturates at higher altitudes. The influence of the angle is visible at all tangent points below 80 km, where the 0° calculation has the highest BT.

It follows that the information in the spectrum at altitudes above 70 km is strongly dependent on the magnetic field parameters. A strong magnetic field will lead to a signal in more filter channels, thus improving the statistics of the measurement. The magnetic strength will furthermore influence the altitude from where the received signal in the center emerges. The angle Φ in combination with the observed linear component of the spectrum can change the observed BT by 100%; thus, at a certain frequency the BT can appear either saturated or not, depending on the observation scenario.

3. Retrieval Technique

The theoretical spectral power, which is measured by the instrument, can be expressed as follows: $F(\mathbf{x}, \mathbf{b})$, where \mathbf{x} denotes the unknown variables, for example, volume mixing ratio profiles and instrument parameters, and \mathbf{b} denotes the constant model parameters, for example, spectroscopic data.

The inverse model I calculates the most likely solution $\hat{\mathbf{x}}$ of the real state \mathbf{x} , which is found in an iterative process. I is a function of a priori information \mathbf{x}_0 and the measurement $\mathbf{y} = F(\mathbf{x}, \mathbf{b}) + \epsilon_y$, where ϵ_y denotes the error in the measurement. The a priori information is also used as the first guess of \mathbf{x} , from which the iterative process starts. They are taken from an atmospheric model; the COSPAR International Reference Atmosphere (CIRA 86) [Fleming et al., 1990] data are used for the calculations presented here.

The optimal estimation method reviewed by Rodgers

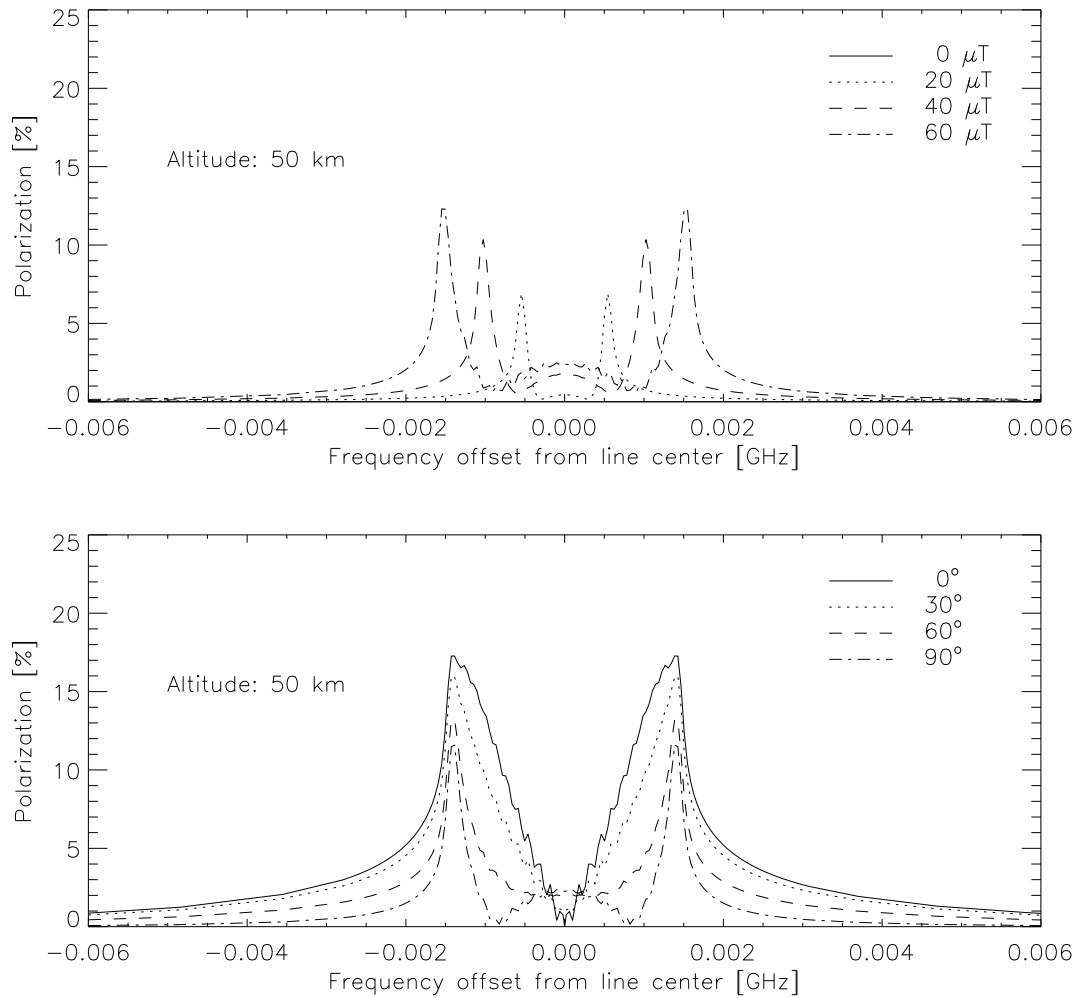


Figure 2. The degree of polarization at a tangent altitude of 50 km for different (top) magnetic field strengths and (bottom) magnetic angles Φ ; the observation scenario is identical to the one used in Figure 1, with either the magnetic strength or angle set constant.

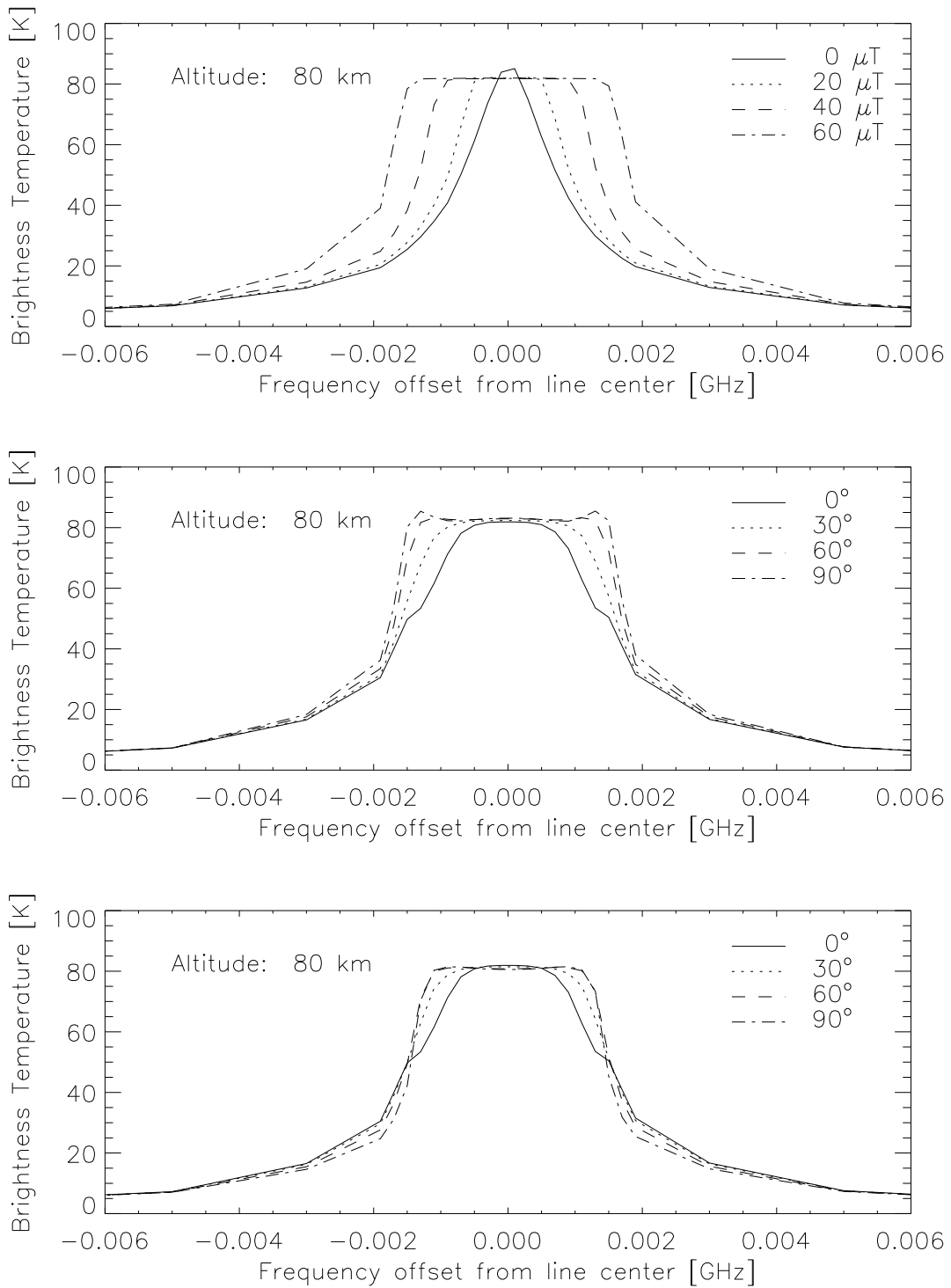


Figure 3. The simulated brightness temperatures at a tangent altitude of 80 km for (top) different magnetic field strengths, (middle) magnetic angles Φ with $\Theta = 0^\circ$, and (bottom) magnetic angles Φ with $\Theta = 90^\circ$; the observation scenario is identical to the one used in Figure 1, with either the magnetic strength or angle set constant.

[1976] is used for the inverse model. Since the problem is nonlinear, an iterative approach using Newtonian iteration is necessary. We can approximate the Forward model by a Taylor series around the point \mathbf{x}_0

$$\mathbf{y} = F(\mathbf{x}_0) + \left. \frac{\partial F}{\partial \mathbf{x}} \right|_{\mathbf{x}=\mathbf{x}_0} (\mathbf{x} - \mathbf{x}_0) = \mathbf{y}_0 + \mathbf{K}_0(\mathbf{x} - \mathbf{x}_0) \quad (7)$$

where $\partial F/\partial \mathbf{x}$ is the Jacobian Matrix. The Taylor series is only calculated up to the first term since the nonlinearity is not very strong.

Rodgers [1976] gives an iteration formula for the calculation of the state $\hat{\mathbf{x}}$

$$\hat{\mathbf{x}}_{n+1} = \mathbf{x}_0 + \mathbf{D}_y[(\mathbf{y} - \mathbf{y}_n) - \mathbf{K}_n(\mathbf{x}_0 - \hat{\mathbf{x}}_n)] \quad (8)$$

with the contribution function

$$\mathbf{D}_y = (\mathbf{S}_0^{-1} + \mathbf{K}_n^T \mathbf{S}_y^{-1} \mathbf{K}_n)^{-1} \mathbf{K}_n^T \mathbf{S}_y^{-1} \quad (9)$$

where $\mathbf{y}_n = F(\hat{\mathbf{x}}_n, \mathbf{b})$, \mathbf{S}_0 is the a priori covariance matrix, \mathbf{S}_y is the error covariance matrix of the measured spectrum, and \mathbf{K}^T denotes the transpose matrix of \mathbf{K} .

In this case, it is not possible to calculate the Jacobian matrix \mathbf{K} analytically; hence a numerical calculation is necessary. This will increase the calculation time proportional to the numbers of iterations times the numbers of retrieved parameters because the major part of the calculation time is used in the Forward model.

The quality of the retrieval can be visualized with the aid of the averaging kernel matrix (AKM) \mathbf{A} . The AKM is calculated as follows: $\mathbf{A} = (\partial I/\partial \mathbf{y}) \mathbf{K}$. A value close to 1 for the corresponding AKM diagonal element of an inversion parameter indicates that the information comes from the measurement; a value close to 0 implies that the inversion parameter is determined by the a priori information. The width of the rows of the averaging kernel matrix gives the smoothing over an altitude range of the inversion parameter.

The error in the retrieval is represented by the statistical error covariance matrix $\hat{\mathbf{S}}$ of the last iteration,

$$\hat{\mathbf{S}} = \mathbf{S}_S + \mathbf{S}_M = [(\mathbf{A} - \mathbf{I})\mathbf{S}_0(\mathbf{A} - \mathbf{I})^T] + [\mathbf{D}_y \mathbf{S}_y \mathbf{D}_y^T] \quad (10)$$

where \mathbf{S}_S is the smoothing error, \mathbf{S}_M is the measurement error, and \mathbf{I} is the identity matrix. The first term in equation (10) represents the smoothing due to the limited altitude resolution of the retrieval and loss of sensitivity, and the second one represents the measurement noise that propagates into the retrieval.

4. Retrieval of Atmospheric Parameters

The temperature profile is retrieved with a vertical resolution of 4–10 km, depending on the altitude. The grid points

have been chosen according to a trade-off between resolution and precision. The vertical resolution of the instrument is limited to 4–5 km, mainly owing to the MAS antenna beam width. The full width at half maximum (FWHM) of the MAS antenna is $\approx 0.4^\circ$, corresponding to ≈ 12 km at the tangent point. Thus it is possible to retrieve temperatures with a grid spacing that is smaller than the FWHM of the antenna, owing to additional information coming from the pressure broadening of the line.

The measurement is truncated to an altitude range from 30 to 110 km for the MAS retrievals, even though the MAS scan range is between 10 and 130 km in vertical steps of ≈ 1 km. This is done for several reasons:

1. Truncated measurements are used to minimize horizontal smoothing. The signal in the center of the line comes mainly from altitudes around 80 km for all tangent altitudes below 80 km (see Figure 1). This gives a good statistic even though the signal is weak. However, it leads to horizontal smoothing of the received signal because the signal comes from different geographic locations. This is a result of the limb scanning technique observing perpendicular to the flight direction.
2. The truncation reduces the influence of the water vapor continuum. The impact of the water vapor continuum is only negligible for tangent altitudes ≥ 30 km because the water vapor contributes to the received signal below 30 km owing to the finite width of the antenna.
3. The signal from the O_2 emission lines above 110 km is too weak.
4. The truncation reduces the computational time.

A mean of the two outermost filter channels left and right from the line center is calculated and subtracted from all measured BT for each individual tangent altitude in the MAS measurement and in the Forward model. This further reduces the sensitivity toward continuum emissions. The bandwidth is sufficiently small to allow a frequency independent subtraction of the continuum. Retrieval of the continuum was avoided to keep the calculations as simple as possible.

We assume the atmosphere to be in hydrostatic equilibrium. The initial temperature profile is taken from the CIRA 86 model. This model gives pressure profiles for altitudes above 20 km only. The initial pressure profile is calculated with the hydrostatic equation by using the initial temperature profile and the pressure given in the CIRA 86 model for an altitude of 20 km. The pressure value at the surface is kept constant during the iterative process, and the retrieval is performed on an altitude grid fixed relative to the surface pressure. The constraint of the pressure initialization at the surface can be balanced by the retrieval algorithm via a different tangent altitude offset. Too high pressure initialization

will result in a positive, too low pressure in a negative, tangent altitude offset.

The width of the received line shape for altitudes > 80 km is influenced by the magnetic field (see Figure 3). Thus it is possible to introduce a magnetic scaling factor in the inversion. This scaling factor adjusts the width calculated with the IGRF model to the width of the line in the MAS data by increasing or decreasing the magnetic field strength. A scaling factor of 1.0 indicates that the line width calculated with the magnetic parameters of the IGRF model agrees with the MAS data. Yet data evaluation exhibited discrepancies between the reproduced spectra and the MAS spectra, where the line width calculated from the IGRF model was up to 10% different from the line width in the MAS data. The source of this error is not clear yet; possible sources might be short-term magnetic field variations, which are not modeled in the IGRF model, or problems in the instrument, for example, frequency stability of local oscillators.

5. Retrieval of Instrument Parameters

Some critical instrument parameters, such as sideband efficiency or tangent altitude offset, have to be retrieved simultaneously with the atmospheric parameters. Information can be obtained from the variation in these retrieved parameters between measurements. Parameters which do not vary with different measurements can be set constant in later retrievals.

The sideband efficiency s_v gives the BT $T_B(IF)$ at the intermediate frequency IF according to:

$$T_B(IF) = s_v T_B^S(LO - IF) + (1 - s_v) T_B^I(LO + IF) \quad (11)$$

where the local oscillator LO frequency for the MAS oxygen channels is at 66.394 GHz. The received BT is a weighted mean of the signal band S and the image band I , according to the principle of a heterodyne receiver, which converts the signal down to the intermediate frequency. For the MAS 9+ line this frequency is ≈ 5.2 GHz; therefore the sideband efficiency will be calculated at this frequency. Typically, two sideband values at the upper and lower frequency border of the line are retrieved, and linear interpolation is used for all frequencies in between.

The sensitivity of the MAS toward the sideband efficiency is high; therefore premission laboratory measurements are not sufficient, and s_v has to be included in the retrieval. The MAS is receiving information of the 9+ line in the signal band around 61.151 GHz and in the image band at 71.637 GHz. The major signal in the image band comes from the wings of the oxygen lines at 60 and 118 GHz and from the water vapor continuum emissions since there are no strong atmospheric lines around 71.637 GHz. This signal is the only source of information about the temperature

profile at altitudes below 20 km since the signal band saturates at ≈ 25 km. The limitation of the measurement to altitudes ≥ 30 km and the continuum subtraction filter out the information coming from the image band. Data evaluation of MAS spectra shows that the retrieved sideband efficiency is constant for all performed inversions and behaves almost like an ideal double-sideband receiver ($s_v = 0.5$).

The determination of the tangent point altitude with the shuttle navigation system is not accurate enough for temperature retrievals. A change of 1 km in the tangent altitude can lead to changes of up to 20% in the simulated BT. A correction to the tangent altitude calculated from the shuttle data was performed [Berg, 1995] by use of the two oxygen lines at 62.998 and 63.569 GHz. This correction is used as the a priori value for a more accurate retrieval of the tangent point position by a tangent altitude offset.

6. Results of Synthetic Retrievals

The synthetic inversions were performed to evaluate the information content of the data and to check the impact of the different parameters on the quality of the retrieval. Investigated parameters were, for example, the magnetic field strength and the angle between magnetic field and observation direction.

The synthetic spectrum was generated by the Forward program, which is used in the inversion calculation as well. Noise has been added to the BT according to the MAS instrument specifications (system noise temperature, 1500 K; integration time, 0.04 s). The magnetic field calculation was performed for the location used in Figure 1. The synthetic measurement represents one MAS scan cycle and consists of 111 spectra for an altitude range from 0 to 110 km in 1 km steps. Each spectrum gives the BT for the 50 filter channels of the 61.151 GHz line. The continuum subtraction (as described in section 4) was applied. The measurement for MAS retrievals was restricted to a tangent altitude range from 30 to 110 km. However, for the investigation of the available information in the spectra, it has been chosen here to use the range 0 – 110 km for the synthetic retrievals to show the possible information that can be gained from an MAS measurement.

An error of 10 K in the temperature was assumed for the calculation of the diagonal elements of the a priori covariance matrix S_0 . The off-diagonal elements, giving information about correlations, have been set to zero. Errors of 1 km in the tangent altitude and 0.1 in the sideband and magnetic scaling factors were assumed. These values reflect the expected variability and act as a limitation to the retrieved values where not enough information is found in the measurement (e.g., temperature at 0 km). These limitations do not

affect the retrieval result if there is sufficient information in the spectrum.

Figure 4 summarizes the result of one inversion. The a priori profile is the CIRA 86 profile for the month of December, latitude 80° ; the true profile is the CIRA 86 profile for the month of June, latitude 45° . The iterative process is stopped when convergence is reached, where the difference between $\hat{\mathbf{x}}_{n+1}$ and $\hat{\mathbf{x}}_n$ (equation (8)) is small. Typically, the inversion converges to the true profile after three iterations; small differences are due to the limited resolution. The side-band efficiency has been initialized with an a priori value of 0.6; the true value of 0.5 is found after two iterations. The tangent altitude offset converges after three iterations. The slightly negative value results from the correlation with the retrieved temperature at 0 km. There is not enough information in the spectrum to retrieve this temperature, so the retrieved temperature comes in part from the a priori, and it is consequently too low. A lower temperature will affect the pressure profile because the pressure is fixed at ground level, and the atmosphere is made hydrostatic with this initial value. The retrieval corrects this by pointing to a lower altitude. The magnetic scaling factor has been initialized with 0.9; the retrieval finds the correct value of 1.0 after four iterations.

Figure 5 (left) shows the smoothing error, the measurement error, and the total statistical error of the temperature retrieval, calculated from the diagonal elements of the matrices \mathbf{S}_S , \mathbf{S}_M , and $\hat{\mathbf{S}}$ according to equation (10). The peak at 24 km results from the saturation of the signal band and to a smaller extent from the smoothing introduced by the profile representation. The information below 20 km comes entirely from the image band; the major error results from the smoothing because the atmospheric temperature profile is only calculated at 0, 10, and 20 km. Temperature profiles of the upper stratosphere and lower mesosphere are obtained with an error between 2 and 3 K. The error increases above 60 km because the information in the line shape is decreasing, and the main information is found in the inner filter channels, which saturate at ≈ 80 km. This and the decreasing vertical smoothing are the reasons for the dip at 80 km. The signal is too weak above 90 km; all the information comes from the a priori, and the error reaches the maximum error given by the a priori error.

The error profile behavior is reflected in the AKM elements, where the rows of the AKM are shown in Figure 5 (right). The AKM element at 0 km reaches a value of 0.3, and the retrieved temperature is a superposition of the a priori and the true value. In addition, the summation of each row is presented by the dotted line, giving a measure about the sensitivity of the retrieval. The sensitivity is high for regions where the summation is ≈ 1 . AKM elements with a

high sensitivity and a sufficient resolution are found in the range from 20 to 90 km.

The restriction of the MAS measurement to a 30–110 km tangent altitude range will lead to the maximum error of 10 K for altitudes below 30 km, and the corresponding AKM element will be almost zero. The AKM elements will not be exactly zero because the measurement at altitudes above 30 km will still provide information about lower altitudes owing to the finite resolution of the antenna. The AKM elements and errors at altitudes > 30 km are almost unaffected.

The influence of the strength of the magnetic field and the angle between observation direction and the magnetic field has been investigated as well. Since the width of the plateau in the middle of the line (see Figure 1) reflects the strength of the magnetic field, the altitude information in the spectrum depends on the magnetic strength.

In Figure 6(left), the error profiles of the 9+ line according to equation (10) have been plotted for four different magnetic field strengths. The maximum error is the a priori error of 10 K. In the case of an unpolarized calculation ($B = 0 \mu\text{T}$), all O_2 molecules absorb at the center frequency, and the inner filter channels saturate at an altitude of ≈ 100 km. The line width is very small, and the statistical information is low, but the error profile exhibits lower errors above 100 km in comparison with the other calculations, owing to the saturation. All the information for altitudes below 90 km is obtained from the line shape, and consequently, the error is large for altitudes of 90–75 km. A magnetic field $> 0 \mu\text{T}$ leads to more information in the range from 90 to 80 km because more filter channels receive a signal. The $20 \mu\text{T}$ calculation possesses the lowest error at 90 km; all the inner filter channels are saturated around this altitude. An increase of the error below 90 km indicates that the information is embedded in the line shape. The saturation point of the line moves farther down with an increase of the magnetic field; the 40 and $60 \mu\text{T}$ calculations saturate around 80 km. The saturation of the line at a certain altitude leads to a shielding of altitudes below the saturation point and to an increasing error. The influence of the magnetic field strength vanishes below 50 km, exhibiting identical error profiles. Information at these altitudes comes from the pressure broadening of the line shape.

The error profiles for different angles between the direction of the magnetic field and the propagation direction for the 9+ line can be found in Figure 6 (middle and right). The 0° calculations result in the same error profile for the $\Theta = 0^\circ$ and $\Theta = 90^\circ$ cases since only the σ lines contribute to the received signal in this observing configuration. The 60° and 90° calculations of the $\Theta = 0^\circ$ case show lower errors for an altitude range from 90 to 50 km because the signal from the σ lines is increasing.

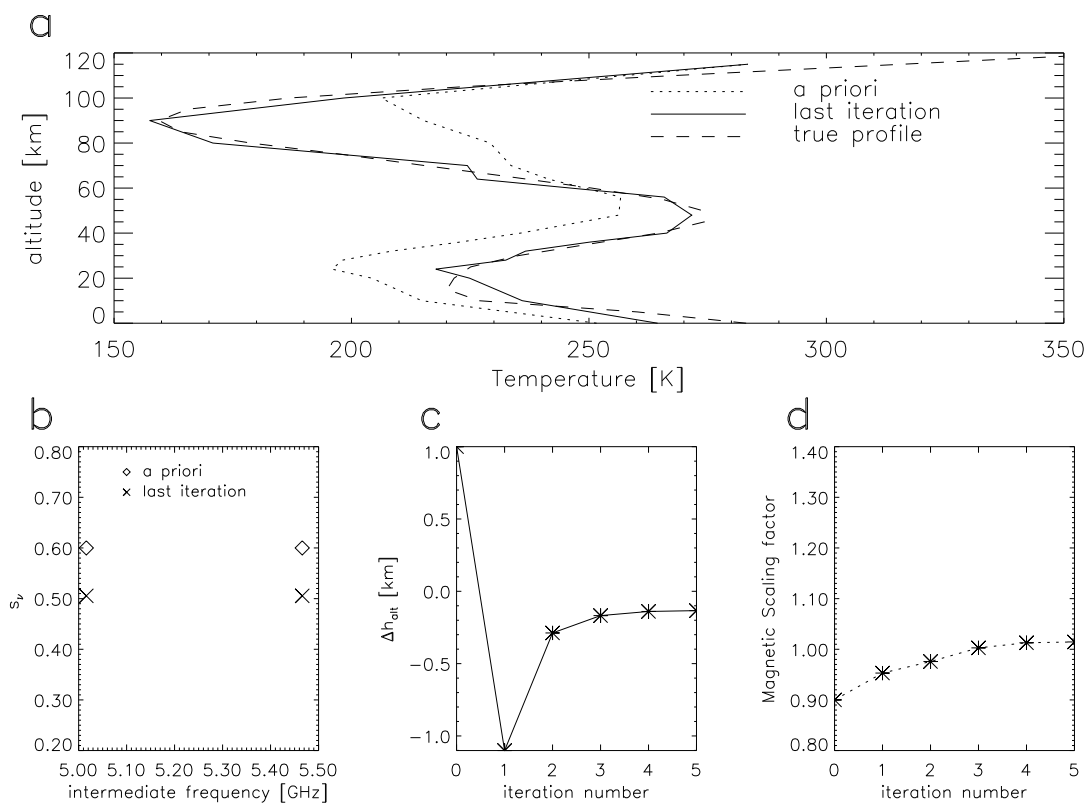


Figure 4. The results of a synthetic retrieval for the 9+ line, including (a): retrieved temperature profile, where the true profile is known, and (b–d): retrieved instrument parameters and magnetic scaling factor. Figures 4b – 4d show sideband efficiency, tangent altitude offset, and magnetic scaling factor, respectively.

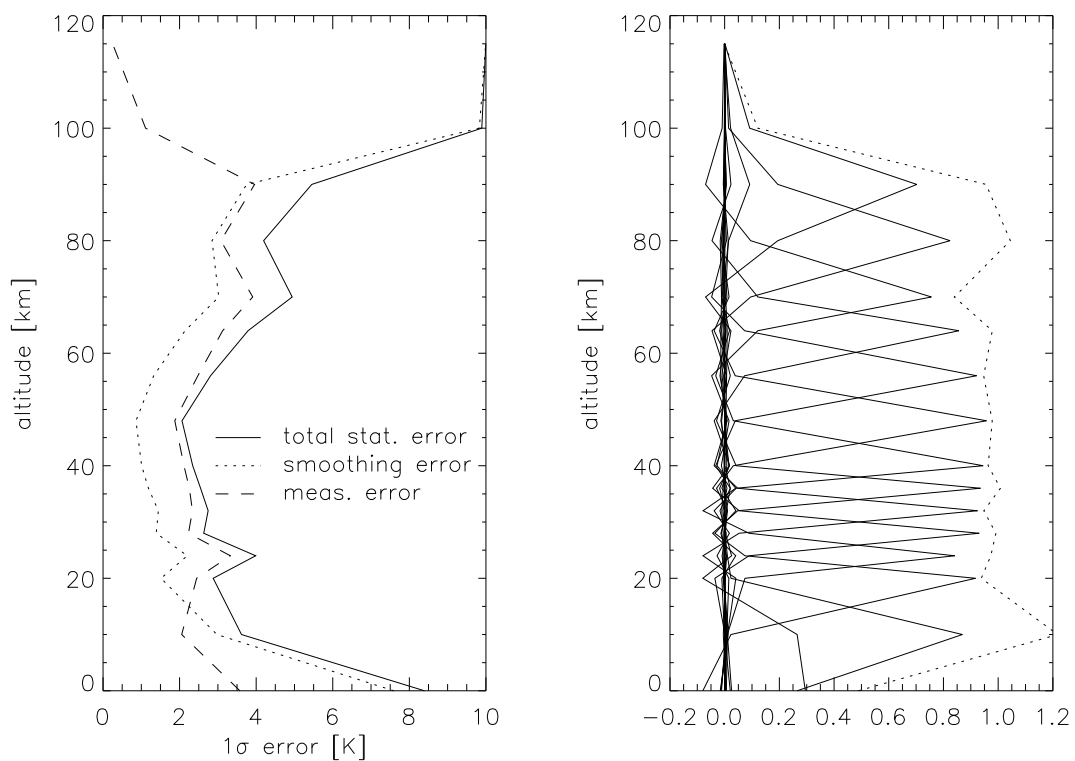


Figure 5. (left) Errors and (right) averaging kernel matrix elements for the synthetic retrieval presented in Figure 4.

The $\Theta = 90^\circ$ case reveals almost no dependence on the angle above 80 km; the signal lies in the inner filter channels, and the polarization is low. An improvement at 70 km is detectable because the σ lines disappear in the wings, and the saturation of the line happens lower in the atmosphere.

7. MAS Results and Comparison With Other Instruments

Five instruments on the Upper Atmosphere Research Satellite (UARS) provide temperature measurements; three of them have been chosen to validate the MAS temperatures. A set of MAS data has been compared to results of the limb-viewing instruments Microwave Limb Sounder (MLS), Cryogenic Limb Array Etalon Spectrometer (CLAES), and Improved Stratospheric and Mesospheric Sounder (ISAMS).

An MAS data set obtained over Saudi Arabia and Iran taken on March 28, 1992, was used for the comparison with the UARS data. The tangent point moved from 7° latitude, 32° longitude to 32° latitude, 56° longitude.

Two UARS limb-viewing tracks close to the MAS limb-viewing track were chosen for the comparison. One track moves from 7° latitude, 44° longitude to 32° latitude, 80° longitude, located east of the MAS measurement; the other one is in the west of the MAS profile locations, moving from 7° latitude, 20° longitude to 30° latitude, 48° longitude. Both tracks were obtained on UARS day 198, corresponding to March 27, 1992.

The profile locations are presented in Figure 7, which also visualizes the different scan scenarios of the instruments. The Universal Time (UT) of the scenarios is indicated. Note that the comparisons include a local time difference of ≈ 6 hours, which will introduce some diurnal temperature variability of 2 K at most [Andrews *et al.*, 1987].

Figure 8 shows the MAS temperature deviations from the CIRA 86 model. The deviations are with respect to the CIRA 86 profile for March, latitude 20° . Five MAS temperature profiles have been smoothed horizontally with a box-car average to get a resolution similar to that of the UARS instruments. The left ordinate shows the data on the original altitude grid, the right ordinate shows the averaged pressures.

Two areas can be identified in Figure 8: an area of smooth variations below 60 km (stratosphere and lower mesosphere) and a highly variable area above 60 km (mesosphere). The stratosphere extends up to ≈ 50 km; the mesosphere extends to 90 km.

The area below 60 km shows rather smooth temperature variations with latitude. Lower mesospheric temperatures around 55 km either agree with the CIRA 86 model or are

slightly above CIRA 86. The MAS detects lower temperatures at 50 km, with deviations of up to 12 K. A layer of enhanced temperature is detected around 40 km. This layer extends over more than 10° latitude. Temperatures below this layer are, in general, lower than the CIRA 86 model except for altitudes close to 30 km. Here the CIRA 86 profile is warmer by ≈ 4 K, but the error of the retrieved profile is higher than that in Figure 5, owing to the truncation of the measurement at 30 km.

Temperatures above 60 km are highly variable with latitude. Generally, the MAS temperatures are below the CIRA 86 model with differences of up to 24 K. The maxima of the difference appear at 70 km, an altitude where the bottoms of temperature inversion layers have been observed by the Halogen Occultation Experiment (HALOE) [Leblanc and Hauchecorne, 1997]. HALOE, another instrument on UARS measuring temperature, observes amplitudes of the inversion layers of up to 14 K, where the maxima occur around the equator for the period of March 1 to May 31, 1992. ISAMS observes amplitudes during the same time of up to 6 K, where one of the maxima is located around 15° latitude and 35° longitude (see Figure 7 by Leblanc and Hauchecorne [1997]). The MAS inversion layers show amplitudes of up to 24 K, where one of the inversion layers occurs at 9° latitude and 32° longitude, near the maxima observed by ISAMS. The amplitude of inversion layers can reach up to 40 K for Lidar observations [Hauchecorne *et al.*, 1987], but satellite measurements observe weaker amplitudes, owing to lower resolution.

The MLS is an instrument using a similar technique as the MAS. A combination of the 15+ and 17+ lines is used for the temperature determination. The Zeeman splitting is included in the calculations, but the MLS has no high resolution filters, which limits the available information to an upper altitude of ≈ 55 km. The temperature below 22 hPa is linearly interpolated from the National Center for Environmental Prediction data; above 0.22 hPa the profile relaxes to the climatology. The MLS data retrieval is performed on a pressure grid. The error of a single profile is 1.5 K at 10 hPa and increases to 3 K at 0.46 hPa [Fishbein *et al.*, 1996]. For a detailed instrument description refer to the work of Barath *et al.* [1993].

The deviations of the MLS temperature measurements from the CIRA 86 model for the month of March, latitude 20° , can be found in Figures 9 and 10, where the MLS data are shown on the original pressure grid (left ordinate) and projected onto an altitude grid using the hydrostatic equation (right ordinate).

The stratospheric MLS temperatures are all below the CIRA 86 model; differences are up to 8 K. The differences increase toward higher latitudes. The layer of enhanced

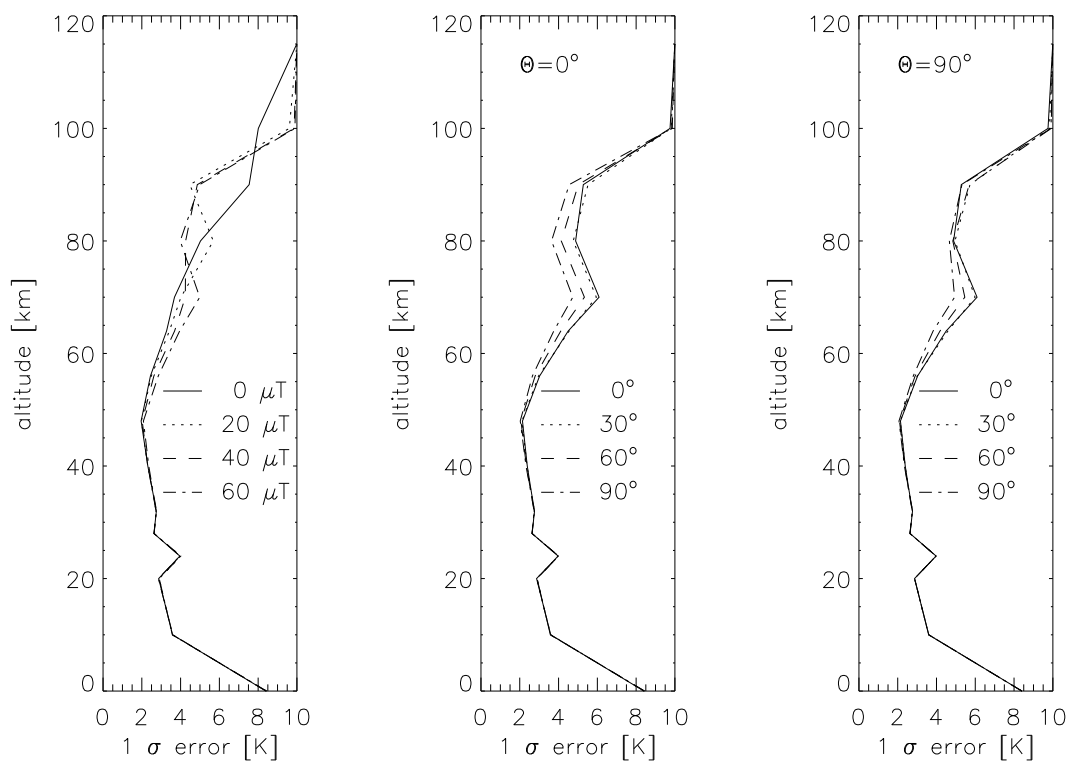


Figure 6. Error profiles for different magnetic field strengths and angles for the 9+ line; the observation scenario is identical to the one used in Figure 1, with either the magnetic strength or angle set constant. Variations shown are of (left) the magnetic field strength and (middle and right) of the angle. The two cases of angle variation are the ones described in Figure 3.

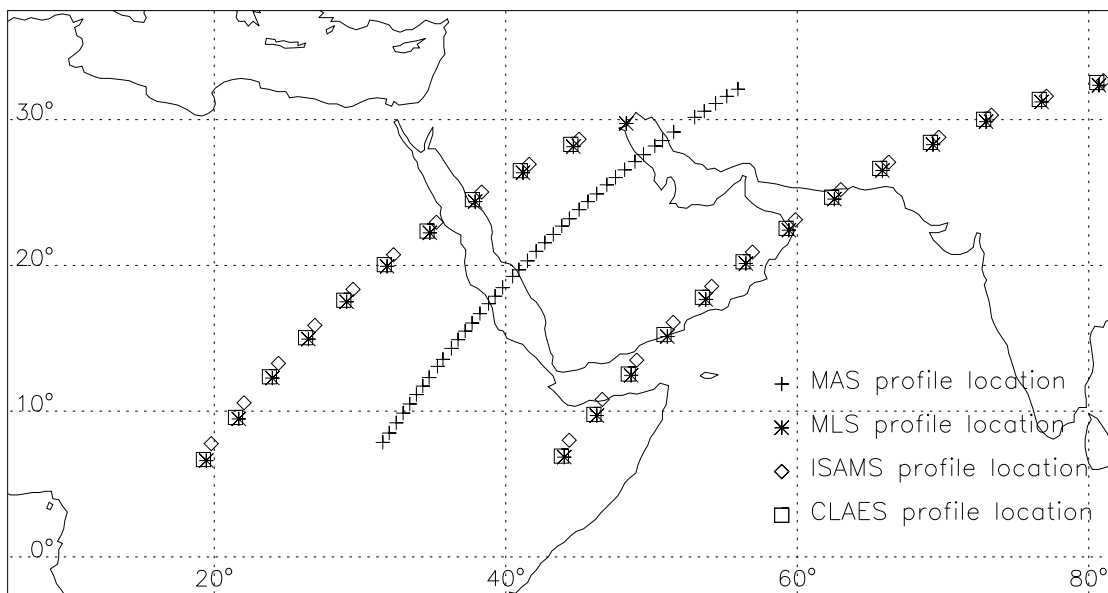


Figure 7. The MAS (March 28, 1992, 0442 UT) and Upper Atmosphere Research Satellite (UARS) (March 27, 1992; east of MAS, 2212 UT; west of MAS, 2343 UT) profile locations over Saudi Arabia and Iran. MLS, Microwave Limb Sounder; ISAMS Improved Stratospheric and Mesospheric Sounder; CLAES Cryogenic Limb Array Etalon Spectrometer.

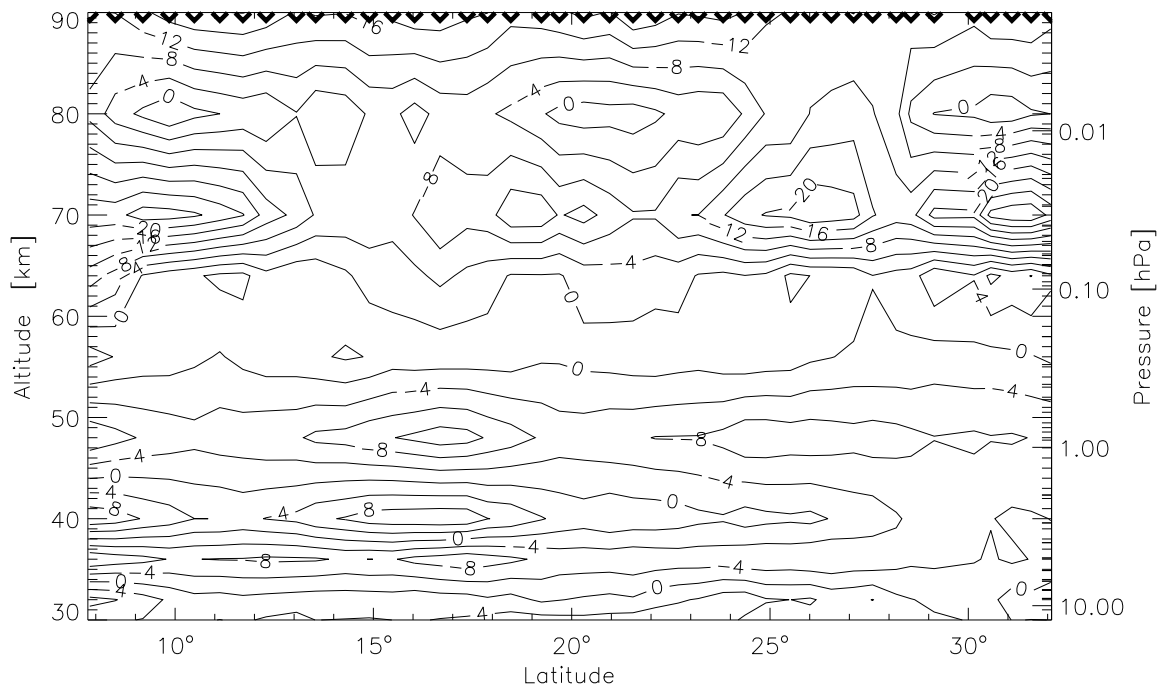


Figure 8. Deviations of the MAS temperatures from the COSPAR International Reference Atmosphere (CIRA 86) temperatures, obtained at 61.151 GHz on March 28, 1992, for the profile locations presented in Figure 7. The tick marks at the top show the positions of the mean latitude of the MAS tangent points.

temperature, visible in the MAS data, is not present in the MLS data. Lower mesospheric temperatures are above the CIRA 86 model at lower latitudes and agree at higher latitudes.

The CLAES instrument measures infrared thermal atmospheric emissions. It obtains temperature profiles by using features of the CO₂ spectrum in the spectral channel at 789–793 cm⁻¹. The principal reference to the CLAES instrument is that of *Roche et al.* [1993].

The temperature deviations from the CIRA 86 model for the month of March, latitude 20°, are presented in Figures 11 and 12. The variations are not as smooth as those in the MLS data, but similar features as in the MLS measurements are observed. The temperatures in the stratosphere are generally lower than those in the CIRA 86 model; lower mesospheric temperatures are above those in the CIRA 86 model.

The ISAMS instrument is an infrared radiometer which uses a combination of interference filters and pressure modulators to select the spectral emissions from the molecules of interest. Emissions from the CO₂ 15 μm vibration–rotation band are used to establish the temperature profiles. The temperature retrieval program uses a combination of sequential and optimal estimation techniques as described by *Rodgers* [1976]. For a detailed instrument description refer to *Taylor et al.* [1993].

The temperature deviations from the CIRA 86 model for the month of March, latitude 20°, are presented in Figures 13 and 14. ISAMS detected lower temperatures than those in the CIRA 86 model throughout the stratosphere. The lower mesosphere has higher temperatures in the CIRA 86 model, while temperatures in the middle mesosphere are below CIRA 86 with deviations of up to 16 K.

8. Conclusion

Synthetic retrievals were performed to verify the inversion method and to investigate the temperature information that can be gained from observation of the 9+ line at 61.151 GHz. The optimal estimation method showed good results for synthetic retrievals, the true profile was found in less than five iteration steps. Simultaneously, instrument parameters were retrieved, which showed convergence within four iterative steps. The optimal estimation method was proven to be a well-suited method to retrieve MAS temperature profiles in the stratosphere and mesosphere.

The performed calculations show the potential of retrieving temperatures up to 90 km when applying the MAS instrument characteristics. Accurate knowledge of the magnetic field and the locations of the tangent point and the instrument are necessary because the magnetic field determines the saturation altitude of the inner filter channels. This

saturation point can vary by more than 10 km for filter channels around the line center and by up to 5 km for the center filter channels for different magnetic fields. The observed linear component of the emitted electric field can influence the error of the obtained profile in the mesosphere by 1.5 K; the influence of the magnetic strength can be as high as 2.0 K.

The error is < 6 K at mesospheric altitudes. Considering that the amplitude of mesospheric temperature inversion layers can exceed 20 K, it follows that the MAS can detect such layers.

The developed software was used afterwards for the retrieval of MAS temperature profiles. The retrieved profiles were compared to data from the UARS satellite.

Two UARS limb-viewing tracks close in time and space of the instruments MLS, ISAMS, and CLAES were used for a comparison with MAS results. Temperature profiles derived from the MAS oxygen line located at 61.151 GHz were compared to the UARS results. Deviation from the CIRA 86 model for the month of March, latitude 20°, were investigated.

All three UARS instruments show lower temperatures throughout the stratosphere, with deviations from the CIRA 86 model of up to 12 K. The MAS shows lower temperatures in the stratosphere as well, with an exception near 40 km and at 30 km. Near 40 km the MAS detects a layer of enhanced temperature, not present in the UARS data. The results at 30 km are less reliable owing to the truncation of the measurement at 30 km. Otherwise, the MAS data agree with the UARS data in the stratosphere.

Lower mesospheric temperatures between altitudes of 50 and 60 km are above the CIRA 86 model with differences of up to 12 K in the CLAES and ISAMS data and up to 8 K in the MAS one. The middle mesosphere is only sampled by one UARS instrument. ISAMS detects lower temperatures than those of the CIRA 86 model; deviations are up to 16 K. The MAS detects lower temperatures of up to 24 K. The major differences in the MAS data occur at an altitude of 70 km, where the bottoms of temperature inversion layers have been observed by the HALOE instrument on UARS. Otherwise, mesospheric temperatures are highly variable with latitude.

The comparison of MAS temperature profiles with data from the UARS instruments MLS, CLAES, and ISAMS shows general agreement. Stratospheric temperatures are generally below those of the CIRA 86 model; lower mesospheric temperatures are above those of CIRA 86. The upper mesosphere is colder than that in CIRA 86 in the ISAMS and MAS data.

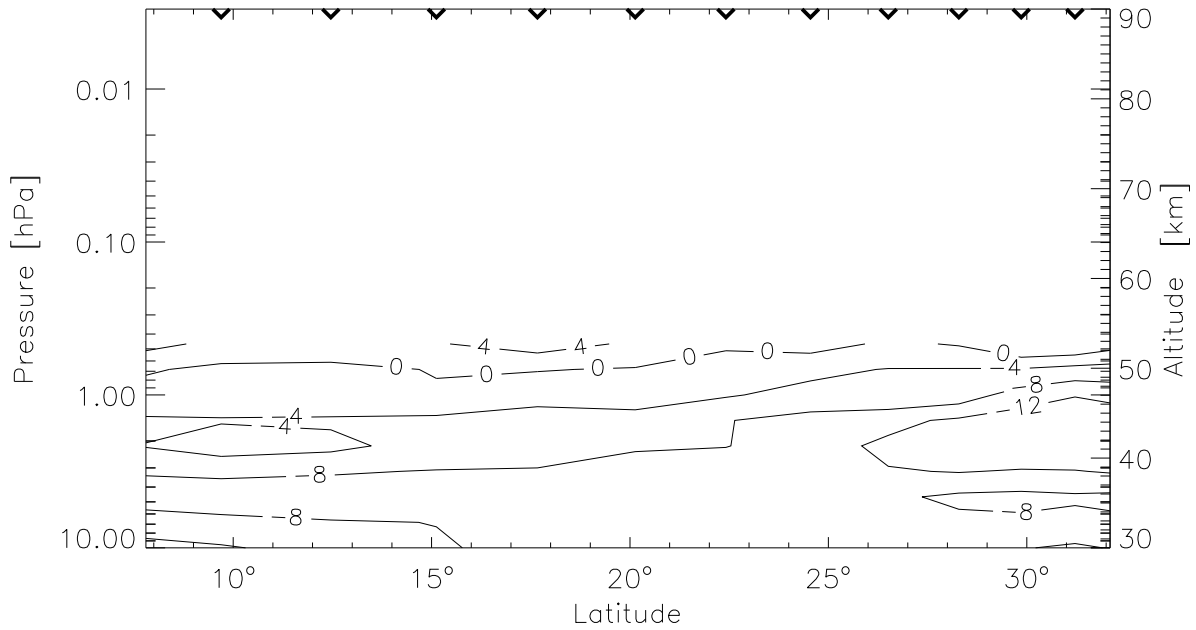


Figure 9. Deviations of the MLS temperatures from the CIRA 86 temperatures, obtained on March 27, 1992 (UARS day 198), for the profile locations presented in Figure 7 (east of MAS). The tick marks at the top show the latitude positions of the MLS profiles.

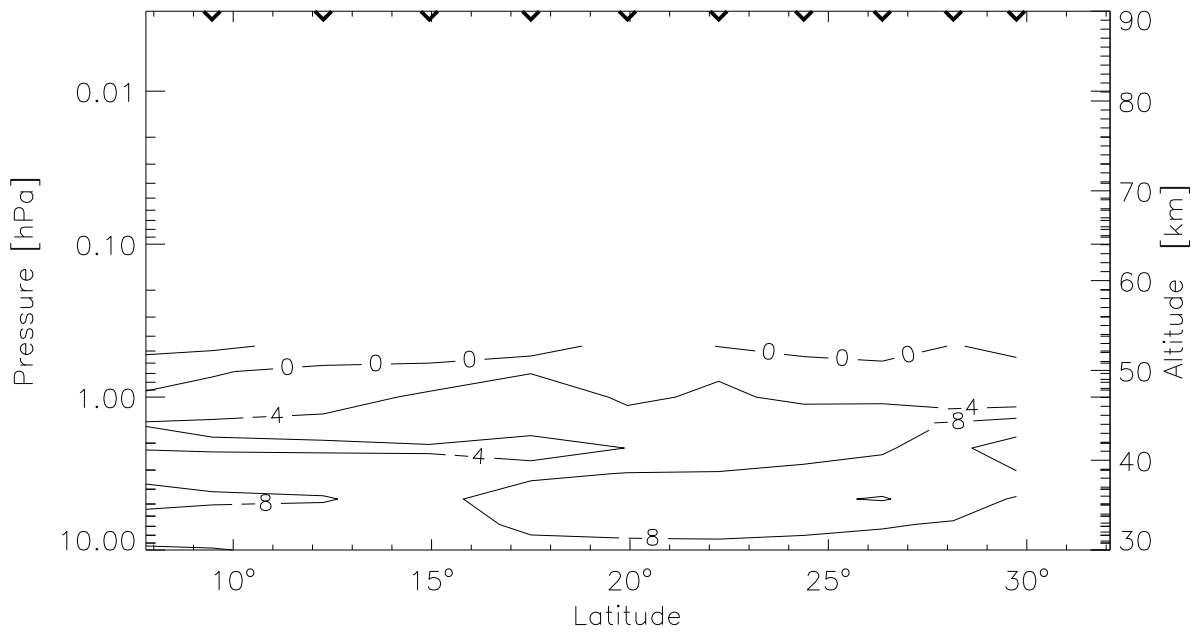


Figure 10. Same as Figure 9 but for profile locations west of MAS.

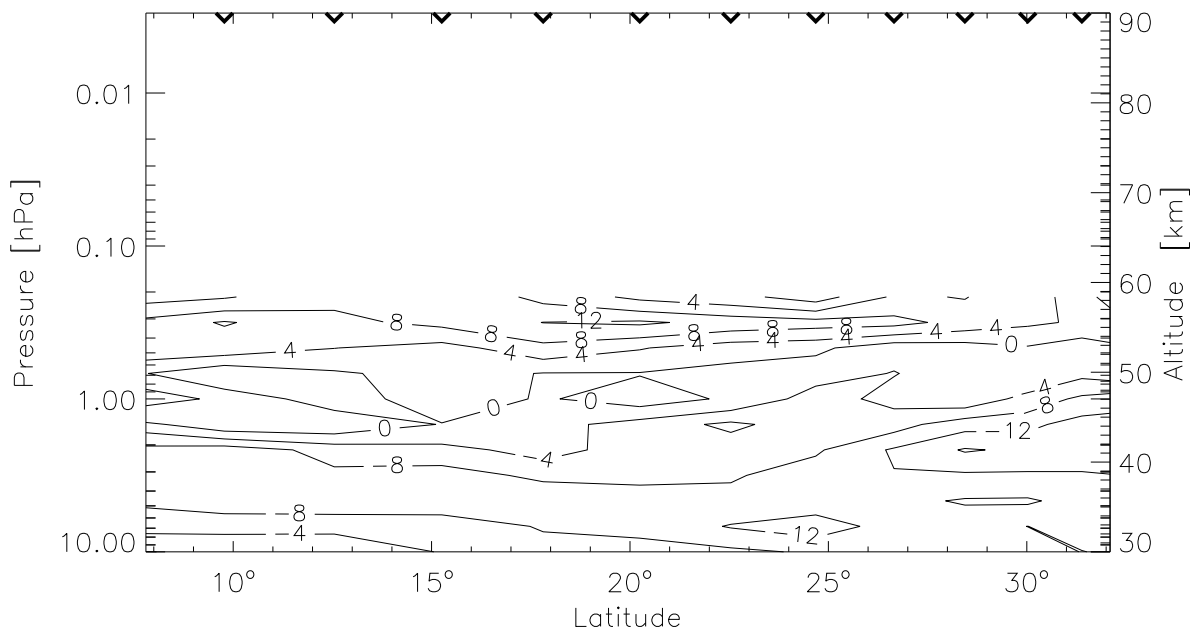


Figure 11. Deviations of the CLAES temperatures from the CIRA 86 temperatures, obtained on March 27, 1992 (UARS day 198), for the profile locations presented in Figure 7 (east of MAS). The tick marks at the top show the latitude positions of the CLAES profiles.

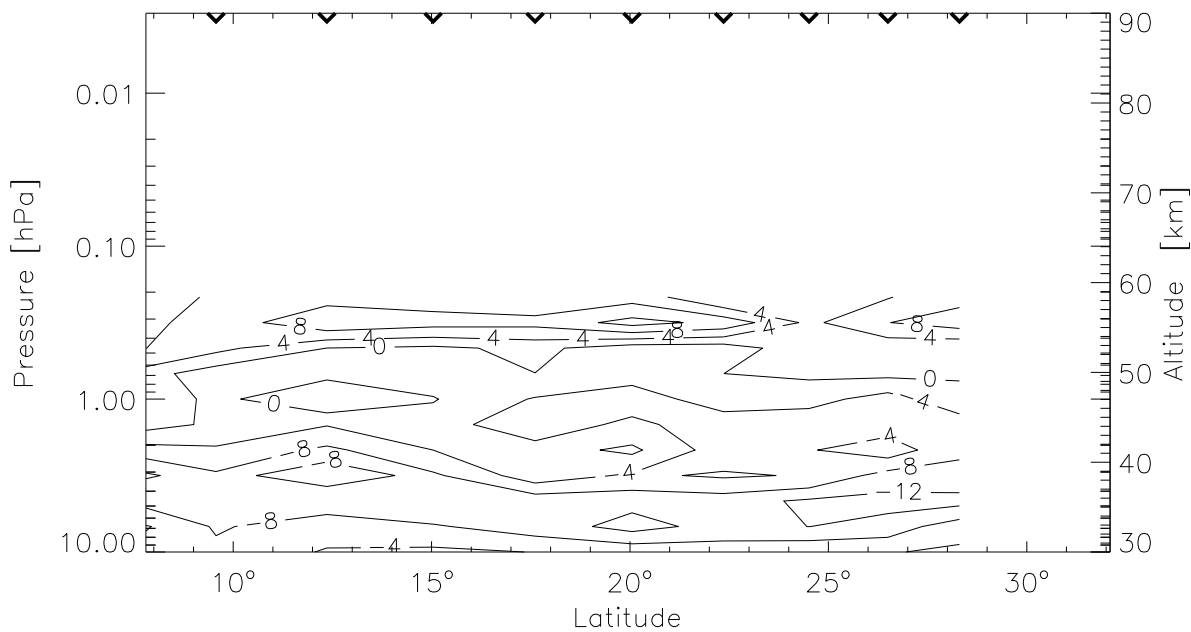


Figure 12. Same as Figure 11 but for profile locations west of MAS.

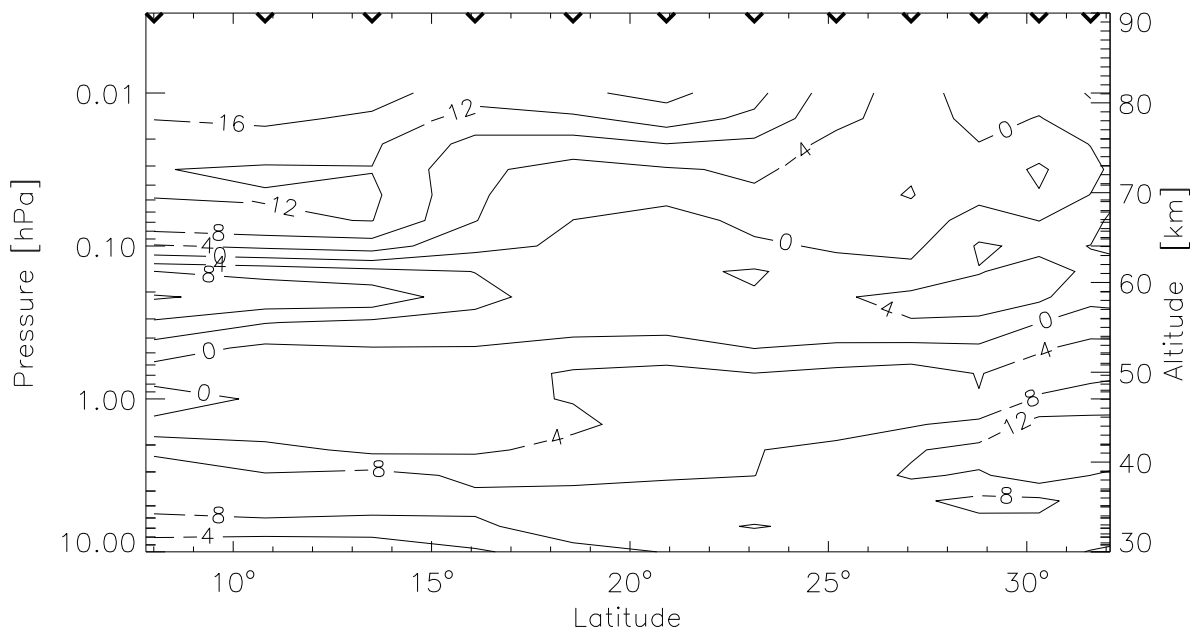


Figure 13. Deviations of the ISAMS temperatures from the CIRA 86 temperatures, obtained on March 27, 1992 (UARS day 198), for the profile locations presented in Figure 7 (east of MAS). The tick marks at the top show the latitude positions of the ISAMS profiles.

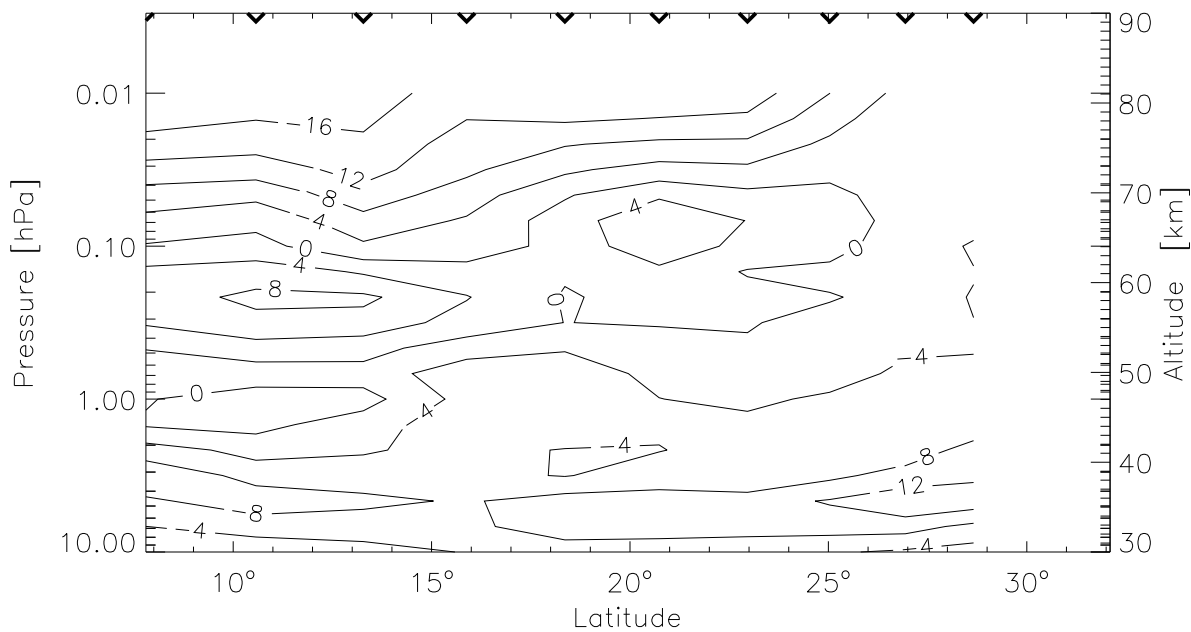


Figure 14. Same as Figure 13 but for profile locations west of MAS.

Acknowledgments A. von Engeln's work was done under the Young Graduate Trainee Scheme at the European Space Research and Technology Center. The authors would like to acknowledge the MAS team, which consists of the groups of G. Hartmann (PI), Max-Planck-Institut für Aeronomie, Germany; N. Kämpfer (Co-PI), University of Bern, Switzerland; R. Bevilacqua (Co-PI), Naval Research Laboratory, USA; C.L. Crosky, Pennsylvania State University, USA; and J. Olivero, Embry Riddle Aeronautical University, USA. The UARS data files were provided by the Goddard Space Flight Center's DAAC. The software used to read UARS data files was developed by H.C. Pumphrey, University of Edinburgh.

References

- Andrews, D., J. Holton, and C. Leovy, *Middle Atmosphere Dynamics*, p. 166, Academic, San Diego, Calif., 1987.
- Barath, F., et al., The Upper Atmosphere Research Satellite Microwave Limb Sounder, *J. Geophys. Res.*, **98**, 10,751–10,762, 1993.
- Barracough, D., International Geomagnetic Reference Field: The fourth generation, *Phys. Earth Planet. Inter.*, **48**, 279–292, 1986.
- Berg, A., Bestimmung des atmosphärischen Druckes mit Hilfe von satellitengetragener passiver Mikrowellenradiometrie, Ph.D. thesis, University of Bremen, Bremen, Germany, 1995.
- Croskey, C., et al., The Millimeter-Wave Atmospheric Sounder (MAS): A shuttle based remote sensing experiment, *IEEE Trans. Geosci. Remote Sens.*, **40**, 1090–1100, 1992.
- Fishbein, E., et al., Validation of UARS Microwave Limb Sounder temperature and pressure measurements, *J. Geophys. Res.*, **101**, 9,983–10,016, 1996.
- Fleming, E., S. Chandra, J. Barnett, and M. Corney, Zonal mean temperature, pressure, zonal wind, and geopotential height as function of latitude, *Adv. Space Res.*, **10** (12), 11–59, 1990.
- Gordy, W., and R. Cook, *Microwave Molecular Spectra*, p. 94, Wiley-Interscience, New York, 1970.
- Hartmann, G., et al., Measurements of O₃, H₂O, and ClO in the middle atmosphere using the Millimeter-wave Atmospheric Sounder (MAS), *Geophys. Res. Lett.*, **23**, 2313–2316, 1996.
- Hauchecorne, A., M. Chanin, and R. Wilson, Mesospheric temperature inversion and gravity wave breaking, *Geophys. Res. Lett.*, **14**, 933–936, 1987.
- Hui, A., B. Armstrong, and A. Wray, Rapid computation of the Voigt and complex error function, *J. Quant. Spectrosc. Radiat. Transfer*, **19**, 509–516, 1978.
- Leblanc, T., and A. Hauchecorne, Recent observations of mesospheric temperature inversions, *J. Geophys. Res.*, **102**, 19,471–19,482, 1997.
- Lenoir, W., Propagation of partially polarized waves in a slightly anisotropic medium, *J. Appl. Phys.*, **38**, 5283–5290, 1967.

- Lenoir, W., Microwave spectrum of molecular oxygen in the mesosphere, *J. Geophys. Res.*, *73*, 361–376, 1968.
- Liebe, H., and G. Hufford, Millimeter-wave propagation in the mesosphere, *Tech. Rep. NTIA 89-249*, U.S. Dep. of Commer., Washington, D.C., 1989.
- Roche, A., J. Kumer, J. Mergenthaler, G. Ely, W. Uplinger, J. Potter, T. James, and L. Sterritt, The Cryogenic Limb Array Etalon Spectrometer (CLAES) on UARS: Experiment description and performance, *J. Geophys. Res.*, *98*, 10,763–10,775, 1993.
- Rodgers, C., Retrieval of atmospheric temperature and composition from remote measurements of thermal radiation, *Rev. Geophys.*, *14*, 609–624, 1976.
- Rosenkranz, P., Absorption of microwaves by atmospheric gases, in *Atmospheric Remote Sensing by Microwave Radiometry*, edited by M. Janssen, chap. 2, pp. 37–90, John Wiley, New York, 1993.
- Taylor, F., et al., Remote sensing of atmospheric structure and composition by pressure modulator radiometry from space: The ISAMS experiment on UARS, *J. Geophys. Res.*, *98*, 10,799–10,814, 1993.
- Wehr, T., S. Böhler, A. von Engeln, K. Kunzi, and J. Langen, Retrieval of stratospheric temperatures from space borne microwave limb sounding measurements, *J. Geophys. Res.*, *103*, 25,997–26,007, 1998.